EUROFUSION WPMST1-PR(16) 14999

M Willensdorfer et al.

Plasma response measurements of magnetic perturbations using electron cyclotron emission and comparison to 3D ideal MHD equilibrium

Preprint of Paper to be submitted for publication in
Plasma Physics and Controlled Fusion

This work has been carried out within the framework of the EUROfusion Consortium and has received funding from the Euratom research and training programme 2014-2018 under grant agreement No 633053. The views and opinions expressed herein do not necessarily reflect those of the European Commission.

Plasma response measurements of external magnetic perturbations using electron cyclotron emission and comparisons to 3D ideal MHD equilibrium

M. Willensdorfer[1]‡, S.S. Denk[1,2], E. Strumberger[1], W. Suttrop[1], B. Vanovac[3], D. Brida[1,2], M. Cavedon[1,2], I. Classen[3], M. Dunne[1], S. Fietz[1], R. Fischer[1], A. Kirk[4], F.M. Laggner[5], Y. Q. Liu[4], T. Odstrcil[1], D.A. Ryan[6,4], E. Viezzer[1], H. Zohm[1], I.C. Luhmann[7], the ASDEX Upgrade Team and the EUROfusion MST1 Team*

[1] Max Planck Institute for Plasma Physics, 85748 Garching, Germany
[2] Physik-Department E28, Technische Universität München, 85748 Garching, Germany
[3] FOM-Institute DIFFER, Dutch Institute for Fundamental Energy Research
[4] CCFE, Culham Science Centre, Abingdon, Oxon, OX14 3DB, UK
[5] Institute of Applied Physics, TU Wien, Fusion@ÖAW
[6]York Plasma Institute, Department of Physics, University of York, Heslington, York,YO10 5DQ, UK
[7] University of California at Davis, Davis, CA 95616, USA
* See http://www.euro-fusionscipub.org/mst1

Abstract. The plasma response from an external $n = 2$ magnetic perturbation field in ASDEX Upgrade has been measured using mainly electron cyclotron emission (ECE) diagnostics and a rigid rotating field. To interpret ECE and ECE-imaging (ECE-I) measurements accurately, forward modeling of the radiation transport has been combined with ray tracing. The measured data is compared to synthetic ECE data generated from a 3D ideal magnetohydrodynamics (MHD) equilibrium calculated by VMEC.

The measured amplitudes of the helical displacement in the midplane are in reasonable agreement with the one from the synthetic VMEC diagnostics. Both exceed the vacuum field calculations and indicate the presence of an amplified kink response at the edge. Although the calculated magnetic structure of this edge kink peaks at poloidal mode numbers larger than the resonant components $|m| > |nq|$, the displacement measured by ECE-I is almost resonant $|m| \sim |nq|$. This is expected from ideal MHD in the proximity of rational surfaces. VMEC and MARS-F calculations reproduce this experimental observation. The calculated poloidal mode structures of the displacement are, therefore, in good agreement with ECE-I measurements.

‡ matthias.willensdorfer@ipp.mpg.de

1. Introduction

The usage of non-axisymmetric external magnetic perturbation (MP) fields is one method, among others, to suppress edge localized modes (ELMs) [1] or to mitigate ELMs [2]. It is utilized in several devices like ASDEX Upgrade [3], DIII-D [4], EAST [5], JET [2], KSTAR [6], MAST [7]. These experiments have shown that ELM mitigation and ELM suppression are achievable over a wide range of collisionalities $\nu^\star$.

At ASDEX Upgrade ELM mitigation using external MPs has been achieved at high plasma densities ($n_{edge}/n_{GW} > 0.65$ corresponding to $\nu^\star > 1.2$)[3, 8] and, more recently, also at low pedestal collisionality $\nu^\star$ ($\nu^\star < 0.4$) [8, 9]. Although large type-I ELMs disappear, small ELMs with frequencies up to 1 kHz remain in both $\nu^\star$ windows. This is different to DIII-D experiments, where ELM suppression with quiescent divertor signals has been achieved. Since the type of the remaining ELMs during the MP phase, especially at low $\nu^\star$, is unclear, we refer to this suppression of large type-I ELM as ELM mitigation.

The low $\nu^\star$ ELM mitigation is accompanied with a decrease of density, the so-called density pump-out [10]. This is also in-line with ELM mitigation experiments in other devices. Density pump-out is observed for ELM suppression in DIII-D indicating a similar underlying physical mechanism for the increased particle transport. More comprehensive experimental studies in ASDEX Upgrade [8, 9], DIII-D [11] and MAST [7] indicate that the degree of ELM mitigation depends on the poloidal spectrum of the applied magnetic perturbation. Moreover, the optimum applied poloidal spectrum for ELM mitigation does not show a maximum of the pitch-aligned magnetic field component. Instead, it is aligned with the mode at the edge that is most strongly amplified by the plasma [7, 11], as calculated with magnetohydrodynamics (MHD) response models like MARS-F [12], JOREK [13] and VMEC [14]. These MHD calculations also suggest that this plasma response is a composition of pressure-driven kink modes and a current driven response referred as the low-n peeling response, which can couple to resonant components [15, 16]. Their individual contributions vary with applied poloidal spectrum of the external magnetic perturbation. Their poloidal mode structures are dominated by poloidal mode numbers m larger than the resonant components $|m| > |nq|$. The kink mode is located around the low field side (LFS) midplane [17, 18], whereas the peeling response is predicted to peak around the X-Point and the top of the plasma [19, 20]. Further experimental investigations indicate that this X-point peeling response, rather than the kink mode at the LFS, causes the ELM mitigation and the density pump-out [7, 9, 11].

The kink response can amplify the external magnetic perturbation, which results in a pronounced non-axisymmetric flux surface displacement at the LFS [21]. Although the kink response seems to play a minor role in ELM mitigation, the effect of this distortion on ELM stability is not completely clear. Moreover, this distortion can also lead to unwanted effects of the position control system on the plasma like unintended movements of the plasma [22]. Hence, it is important to measure it and to compare it

to MHD codes.

In this paper, we describe a method to measure the non-axisymmetric flux surface distortion using toroidally localized electron cyclotron emission (ECE) measurements and rigid rotating $n = 2$ MP-field. A similar method has already been used in Refs. [23, 24] to compare the kink response of DIII-D plasmas with IPEC calculations [25]. We extend this method using the electron cyclotron forward modeling from Ref. [26] and additional ray tracing, which provide the accuracy needed to study the kink response at the edge. To allow comparisons with the 3D ideal MHD equilibrium calculations from VMEC [27], we developed synthetic VMEC diagnostics. In case of the synthetic ECE data, we combined the forward modeling and the 3D equilibrium from VMEC.

The amplitude of the plasma surface distortion and the poloidal mode structure are quantitatively compared. Additional profile diagnostics like the lithium beam (LIB) and charge exchange recombination spectroscopy (CXRS) as well as MARS-F calculations complement the comparison.

This paper is organized as follows. Section 2 describes the measurement principle, the experimental setup, the magnetic perturbation coil setup and the diagnostic tools with focus on ECE diagnostics. The forward modeling of the ECE systems is presented in Section 3. The VMEC calculations and the implementation of synthetic diagnostics are explained in Section 4. Section 5 and 6 present the comparison of the amplitude and of the poloidal mode spectrum, respectively. Conclusions and a summary are given in Section 7.

2. Experimental setup

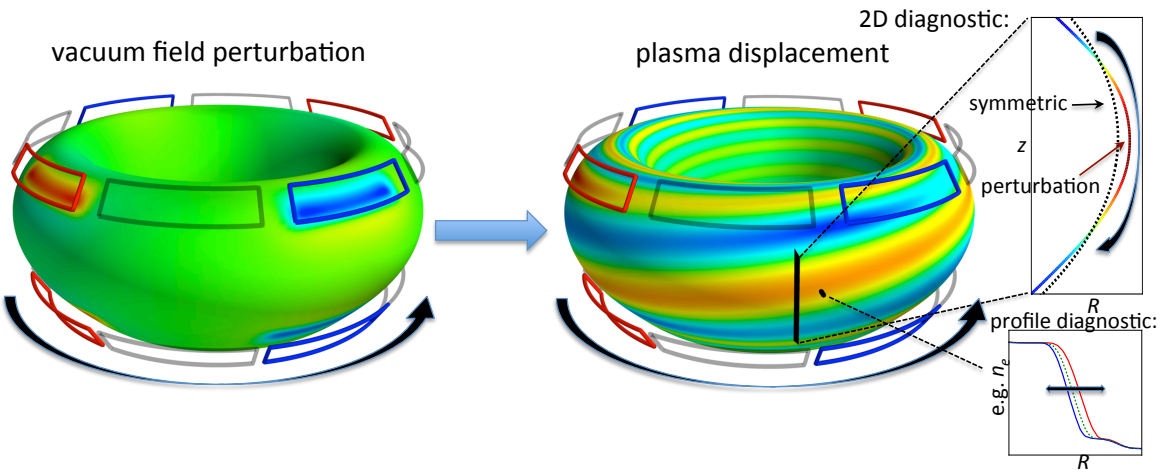

Figure 1. Cartoon of measuring the plasma displacement using rigid rotation of the MP field. External saddle coils produce magnetic perturbations of the vacuum field (left), which results in a perturbation of the flux surfaces (middle). A rotation of this external field results in a rotation of the displacement, which can be measured by an imaging system (right, top) or profile diagnostics (right, bottom). The rotation in the direction of positive toroidal angle ϕ is indicated by arrows.

The measurement principle is based on external saddle coils, which produce non-axisymmetric MPs in the vacuum field. The result is a more or less field aligned non-axisymmetric distortion of the flux surfaces. The main idea is that a rotation of this external MP-field leads to a rotation of the displacement (illustrated in Figure 1). This rotating distortion is then measured by profile and/or imaging diagnostics [18]. In profile diagnostics, the rotating distortion should appear as radially varying displacement and their high spatial resolution can be used to accurately measure the amplitude of the distortion [28, 29]. From the imaging diagnostics, we can gain information about the alignment of the distortion by inspecting the poloidal phase of the plasma response as a function of the continually varied toroidal phase of the applied magnetic perturbation. The present experiment was made with the toroidal magnetic field and plasma current pointing in opposite directions, hence negative safety factor q. Consequently, an imaging system should detect a poloidally downward propagating structure, if the rotation is in positive toroidal direction (counterclockwise in the cartoon). The rotation directions are indicated by arrows in Fig. 1.

In this paper, we focus on ECE diagnostics for profile and imaging measurements. They are ideal to track changes of the flux surfaces, since they are able to deliver electron temperature (T_e) with high temporal resolution. Due to the very large electron heat diffusivity along the magnetic field, T_e is essentially constant on flux surfaces.

2.1. MP-coils and edge diagnostics

ASDEX Upgrade is equipped with 16 MP-coils, which are arranged in two poloidally separated rows and each has eight toroidally equidistant coils [30] (shown in figure 2). This allows us to apply an MP field with a toroidal mode number n of 1, 2 and 4. A newly installed power supply system enables us to rotate the MP field of the two coil sets separately [31]. Thus, it is possible to employ either a differential rotation (sets in different direction) or a rigid rotation (both sets in same direction) with $n = 1, 2$ with frequencies up to several 100 Hz [31]. Because of the passive stabilization loop (PSL) conductors in ASDEX Upgrade, fast rotating fields are attenuated and delayed by image currents [32]. To avoid significant attenuation, we applied a low frequency of 0.5 Hz for the $n = 2$ rigid rotation in even parity configuration. The resulting attenuation is not more than 10%. Even parity configuration means that the differential phase angle between the field of the upper and lower coil $\Delta\phi_{\mathrm{ul}}$ is 0° [33]. Since there are 8 saddle coils in each row, the toroidal mode spectrum of the applied vacuum fields exhibits a dominant $n = 2$ and weak $n = 6, 10, 14, \ldots$ components but no other additional side bands. The intrinsic error field for $n = 2$ is assumed to be small, because: First, no global density perturbation have been observed during $n = 2$ rigid rotation Second, dedicated measurements of the $n = 1$ error field also indicates a small $n = 2$ component (no ellipse in Fig. 4 in Ref. [34]).

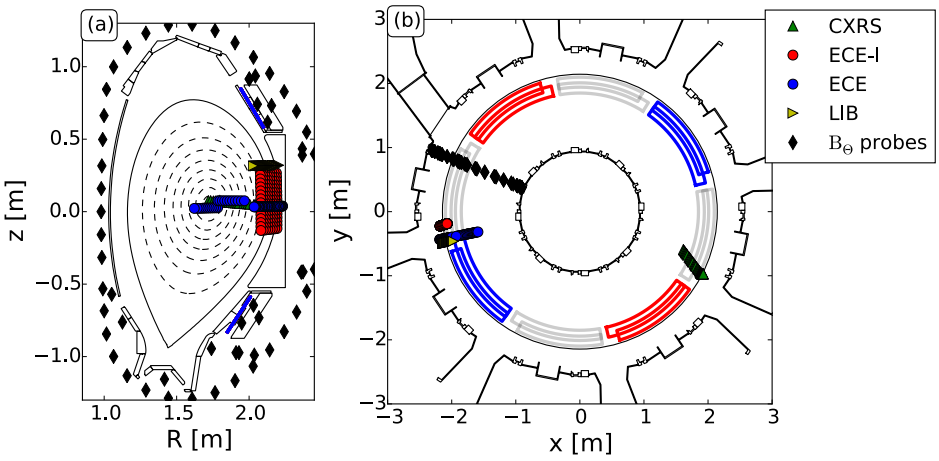

Figure 2. Overview of the used diagnostics and the MP-coils using (a) poloidal and (b) toroidal cut. Color scaling of the MP-coils indicate an $n = 2$ perturbation.

To obtain the edge displacement accurately, several high resolution edge diagnostics are in use. Figure 2 shows the poloidal (2(a)) and toroidal (2(b)) positions of CXRS [35], LIB [36, 37], ECE and ECE-imaging (ECE-I), which measure ion temperature (T_{i}), electron density (n_{e}) and T_{e}, respectively. Additionally, the magnetic probes used for equilibrium reconstruction and plasma position control are shown.

In this paper, we mainly analyze ECE measurements to track changes in the magnetic structure. To obtain reliable edge profiles of T_{e} from ECE, it is necessary

to forward model the electron cyclotron radiation transport [26]. The 1D-profile ECE diagnostic (blue circles in Fig. 2) uses a heterodyne radiometer with 60 channels and a sampling rate of 1 MHz. At the standard magnetic toroidal field configuration of $B_\mathrm{T} \sim -2.5$ T, 36 channels cover the edge region with a spatial resolution of about 5 mm. This spatial resolution is set by the frequency spacing between the channels, the intermediate frequency (IF) bandwidth of 300 MHz of each channel and the additional broadening due to electron cyclotron radiation transport effects like Doppler broadening. The remaining 24 channels are used to measure the core using a frequency spacing of ~ 1 GHz and an IF bandwidth (f_IF) 600 MHz resulting in a spatial resolution of about 12 mm. The 1D-profile ECE system is calibrated absolutely [38, 39], whereas the ECE-I system relies on a cross calibration.

The used ECE-I system has 128 channels with a temporal resolution of 200 kHz [40] and was configured to cover the plasma edge. It has 16 rows with a vertical spacing of ~ 25 mm and 8 channels in each row. The frequency spacing is 800 MHz, whereas f_IF is 700 MHz. The resulting radial spatial resolution is around 15 mm at the edge. The advantage of ECE-I is that the vertical distribution of the channels allows us to resolve poloidal structures. Because of a recent extension to a quasi 3D system [41], the toroidal angle between the geometrical lines of sight (LOS) of the ECE-I system and the toroidal field is oblique. This complicates the interpretation of the ECE-I system and it is necessary to forward model the ECE-I. This is treated in detail in section 3.

Measuring the 3D displacement using toroidally localized diagnostics and a rigid rotating field is based on two assumptions: First, the measured plasma parameters are constant on the perturbed flux surfaces and second, global plasma parameters, like core temperature and density, do not change significantly during the rigid rotation. The validity of both assumptions is justified in the following section.

2.2. Discharge

The presented experiment at ASDEX Upgrade was done at a plasma current of $I_P = 800$ kA and a toroidal field of $B_\mathrm{T} = -2.5$ T (direction of B_T is clockwise). In this configuration, the direction of the ion ∇B drift is towards the X-point and the edge safety factor amounts to $q_{95} \sim -5.2$. Figure 3 shows the time traces of global plasma parameters during the application of the MP coils. The rotation was performed with a frequency of 0.5 Hz indicated by the MP coil current (Fig. 3(a)). Two periods in positive toroidal direction were performed and in-between the neutral beam injection (NBI) power was stepped from 5 to 7.5 MW. Within one NBI step, the density and temperature do not vary more than 6% in the core (Fig. 3(b,c)). The normalized beta β_N amounts to ~ 1.7 and ~ 2 in the second NBI power step. The application of this MP coil configuration does not significantly affect the ELM behavior as seen in the divertor current (Fig. 3(f)). ELM mitigation is not expected for these parameters with an even parity configuration ($\Delta\phi_\mathrm{ul} \sim 0°$). The optimum phase angle for ELM mitigation for this high B_T and high q case scenario is, according to MARS-F [12] calculations,

$\Delta\phi_{\mathrm{ul}} \sim -90°$ (Fig. 11 in Ref. [20]).

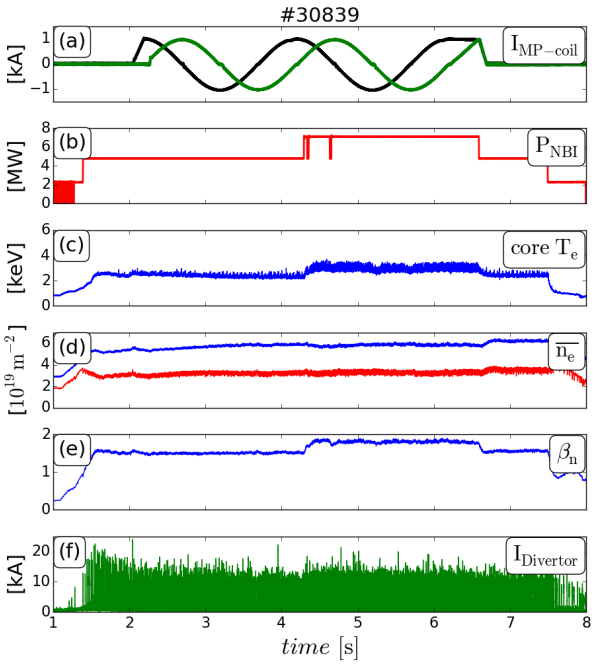

Figure 3. Discharge overview, (a) coil current for the MP coils indicating the rigid rotation, (b) heating power, (c) core electron temperature, (d) line integrated density of core and edge chords, (e) normalized beta β_N and (f) divertor current. The rigid rotation does not alter global plasma parameters.

It is clearly seen in Figure 3 that core densities and temperatures do not change significantly during the rigid rotation (less than 6%). This confirms the assumption of constant global plasma parameters. The time traces of Figure 3 also suggests that the first assumption of constant measured plasma parameters on perturbed flux surfaces in the pedestal region is fulfilled. The breaking up of flux surfaces due to stochastization in the bulk of the pedestal would result in a significant decrease of the temperature and density gradients in the pedestal and, consequently, also of core temperatures and density. Since there is no pronounced drop of these parameters during the switching on of the MP field, a stochastization of the entire gradient region can be ruled out. Strike point splitting [42] is observed and indicates a break in axisymmetry. But there is no hint for stochastization within the edge region. Moreover, we can also assume that ideal MHD is applicable in this case, which is discussed in section 4.2.

2.3. Edge measurements during rigid rotation

Although core n_e, T_e and T_i values are almost constant in time, every edge diagnostic observes a radial position shift due to the rigid rotation of the MP field. Time traces from ECE, ECE-I, LIB and edge CXRS in Fig. 4 show a clear modulation due to the radial shift. To visualize the modulation, we use only data from pre-ELM time points. The differences between raw data and ELM synchronized data using ECE measurements

are shown in Figure 4(b).

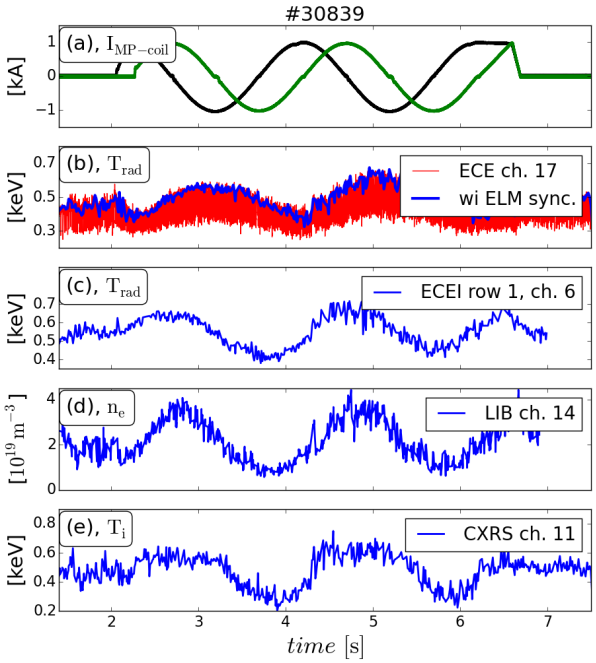

Figure 4. Edge measurements during the rigid rotation: (a) coil current of the MP coils indicating the rigid rotation, (b) one edge ECE channel with and without ELM synchronization, (c) ELM synchronized ECE-I channels, (d) edge LIB and CXRS. The edge perturbation is seen in each edge diagnostic.

To demonstrate that the MP field perturbs the entire edge profile, Figure 5 shows one edge n_e profile before the MP onset and two profiles at different toroidal phases during the rigid rotation. These edge profiles exhibit a significant change in the real space gradients, whereas pedestal top values remain nearly the same for all three cases. This indicates that the MP field induces flux surface expansions and compressions, which depend on the toroidal phase.

In addition to the toroidal symmetry breaking, the MP-field also adds poloidal structures. This is expected from various plasma response calculations [43] and is observed by the ECE-I system. Figure 6(a) shows the mean radiation temperature during the rigid rotation using the cold resonance positions for the mapping (details in Section 3). The solid line indicates the last closed flux surface (LCFS) and the dashed line a flux surface within the pedestal region at a normalized poloidal flux of $\rho_{pol} \sim 0.972$ (The used definition of ρ_{pol} is in Ref. [44]). ELM synchronized time traces of channels along this flux surface and a least square (LSQ) fit of a sine function including their higher harmonics are shown in Figures 6(b). The modulation is observed in each of these channels. Furthermore, this modulation is propagating downwards as expected from a MP-field rotation in positive toroidal direction (see Fig. 1 for illustration).

ECE-I measurements during the rigid rotation contain valuable information about the flux surface displacement. The perturbation is usually characterized using the Fourier decomposition of its normal component $\xi_r = \xi_a \, e^{i(m\Theta^\star - n\phi)}$, where ξ_a is the

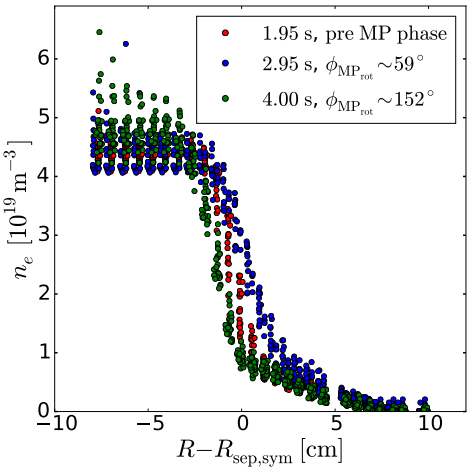

Figure 5. Edge n_e profiles from the LIB diagnostic versus R relative to the axisymmetric separatrix. The edge gradients in real space are changing suggesting a flux surface expansion and compression during the rotation.

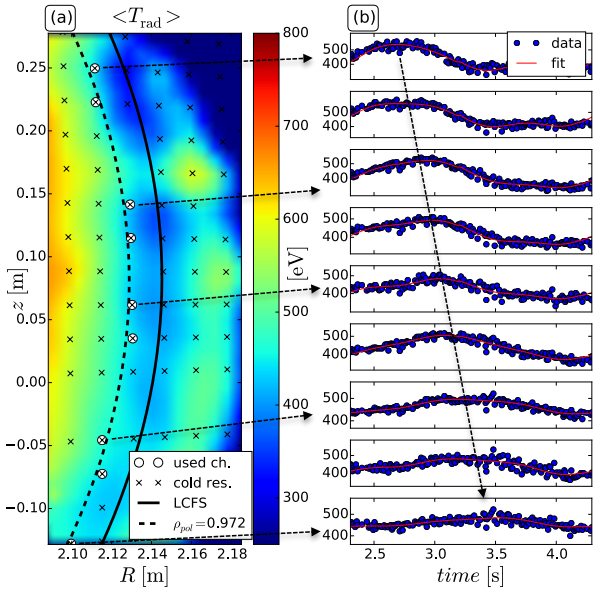

Figure 6. (a) The color code shows the mean of radiation temperature $< T_\mathrm{rad} >$ throughout the rigid rotation ($t \sim 2.2 - 4.4$ s) using the cold resonance positions of the ECE-I channels (crosses). Circles indicate channels close to a flux surface in the pedestal $\rho_{pol} \sim 0.972$. The lines indicate a flux surface in the pedestal $\rho_{pol} \sim 0.972$ (dashed) and the last closed flux surface (solid). (b) Time traces of T_rad and their corresponding LSQ fit from channels marked as circles in (a). The modulation is propagating downwards.

amplitude, n the toroidal mode number, ϕ the toroidal angle, m the poloidal mode number and $\Theta^\star$ the straight field line angle. ξ_r directly measures the displacement between the axisymmetric and 3D surface [14]. Because of its poloidally and radially localized channels, the ECE-I diagnostic is able to resolve the poloidal mode numbers m. One can obtain m using $m = \frac{\Delta\Theta^\star}{\Delta\phi}$, where $\Delta\phi$ and $\Delta\Theta^\star$ are the toroidal phase increment

and the corresponding straight field line angle difference between the various ECE-I channels. Therefore, the determination of m depends strongly on the accuracy of the calculated straight field line angle. Because of the high shear in the pedestal region, the calculation of $\Theta^\star$ is very sensitive to the used flux surface. The correct positions and the corresponding flux surfaces of the ECE-I channels are therefore essential to determine the poloidal mode structure accurately. To provide accurate measurement positions of the ECE-I channels, we applied forward modeling of the radiation transport, which is described in the next section.

3. Interpretation of ECE

The ECE-I diagnostic was extended to allow quasi 3D measurements using a second ECE-I system, which was not in use at the time of this experiment [41]. Because of the new requirements, it was necessary to change the LOS geometry. This increased the toroidal inclination angle $\angle$ between the LOS and the normal to flux surface or rather the toroidal magnetic field. Therefore, the LOS are oblique and not perpendicular anymore. This additional angle enhances the Doppler shift of the observed ECE intensities and their origin can significantly differ from the cold resonance position. This section describes the determination of the position of the observed ECE intensity needed for the ECE-I system. This analysis was done for a time-point prior to the MP onset, hence, axisymmetry is assumed.

3.1. Definition of the 'warm' resonance position

T_e is routinely determined from the radiation temperature (T_rad) of the 1D ECE measurements using a forward model within the framework of integrated data analysis (IDA)(details in [26, 45]). The T_e profile is varied until the most likely match between measured and estimated ECE intensity within the Bayesian analysis is found. The ECE intensity is calculated by solving the radiation transport equation along the LOS [26] of the ECE diagnostic for given T_e and n_e profiles. Because we are mainly interested in the origin of the observed intensity, we only use the module of IDA, which solves the radiation transport equation. For this purpose, T_e and n_e profiles from routine IDA evaluation serve as input [44].

To account for additional refraction, we extended the modeling by ray tracing [46], which is found to be in good agreement with the TORBEAM code [47]. The ray tracing code calculates the ray path of each channel until the ray hits the wall [46]. Then, the radiation transport equation is solved along the ray path starting from the end of the ray towards the diagnostic antenna. The combination of forward modeling and ray tracing allows us to determine exactly the origin of the observed intensity. The distribution of the observed intensity (D_ω) [45] is the normalized product of the emissivity $j_w(s)$ and the transmittance $T_\omega(s)$ along the ray path coordinate s:

$$D_\omega(s) = \frac{j_w(s)\ T_\omega(s)}{\int j_w(s)\ T_\omega(s) ds} \tag{1}$$

Figure 7 illustrates the calculated emissivity, transmittance (Ref. [45]) and the resulting D_ω for one 1D-ECE channel in the pedestal region. Although we neglect the IF bandwidth, the calculated D_ω is relatively broad, which is attributed to the Doppler and the relativistic broadening.

To have a single quantity as an approximation for the measurement position of a single ECE channel, we use the maximum of D_ω labelled as 'warm' resonance position [48] (shown in Fig. 7). The 'warm' resonance position can differ from the cold resonance position indicated by the vertical lines in Figure 7(b). This discrepancy originates from

Doppler effects due to an oblique LOS of $\angle \sim 8.6°$. Although the toroidal inclination angle of the profile ECE system amounts to only $\sim 4°$ and almost no poloidal inclination angle, additional refraction by the plasma leads to an even larger angle at the cold resonance position. As a result, the Doppler shift becomes more important, especially, in the case of the ECE-I system.

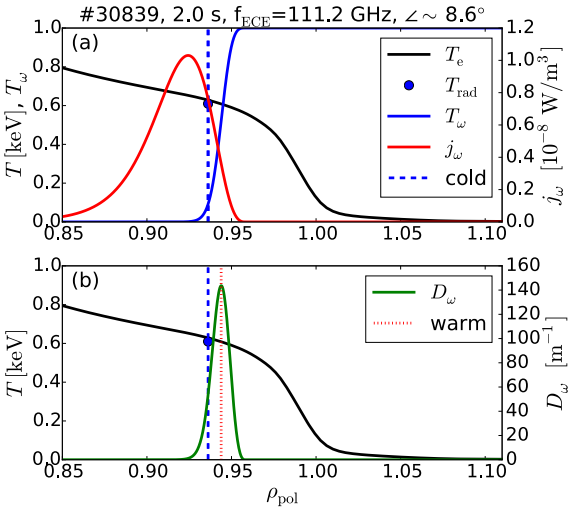

Figure 7. (a) emissivity j_ω and the transmittance T_ω are shown along the ray path mapped on ρ_{pol}. (b) The distribution of the observed intensity (D_ω) and its maximum, the 'warm' resonance position is indicated by a vertical dotted line. In both frames, the used T_e profile (solid, black) and the cold resonance position (vertical dashed) are shown.

3.2. Forward modeling of the ECE-I data

Because of a toroidal inclination angle at launch of $\angle \sim 7.2°$ and additional poloidal angles, the Doppler shift influences the ECE-I even more than for the profile ECE system. Fig 8(a) and (b) show a comparison between the D_ω of one 1D-ECE channel and one from the ECE-I system at similar (R, z) cold resonance positions. For the shown ECE-I channel, refraction causes an angle of $\sim 17.7°$. This leads to a significant broader D_ω and to an even larger shift between the cold and 'warm' resonance (15 mm).

Figures 8(c) and (d) present the modeled radiation temperature at their cold resonance position from all profile ECE and ECE-I channels covering the edge, respectively. Additionally, Fig. 8(c) also shows the absolutely calibrated ECE measurements, which underlines the correct description of these measurements. In the far scrape off layer (SOL) ($\rho_{\mathrm{pol}} > 1.05$), the measurements deviate from the model. These channels are so optically thin that wall reflections are becoming important. Because of its additional complexity, wall reflections are not considered.

The well-known shine-through peak appears in both systems [49] and it is even more pronounced in the ECE-I system due to their oblique LOS. Furthermore, T_{rad}

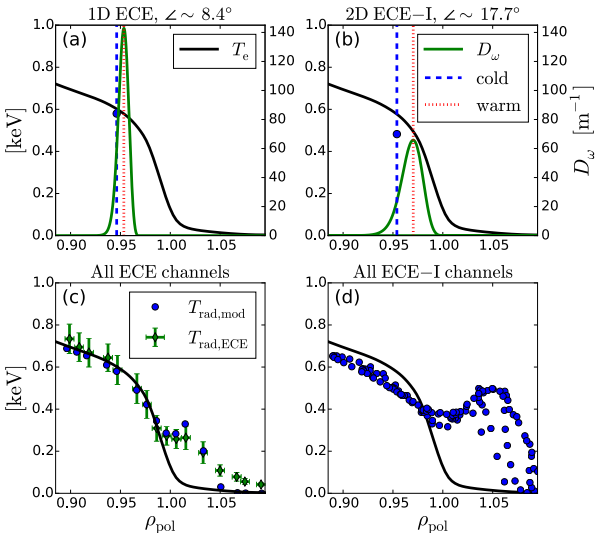

Figure 8. Discharge #30839 at 2.0 s, (a) D_ω from an 1D-ECE channel at the pedestal top is shown. Cold and 'warm' resonances are indicated by vertical dashed and dotted lines, respectively. The modeled T_{rad} is shown at the cold resonance position as blue circle. (b) same as (a) for an ECE-I channel at similar position. (c) modeled (circle) and measured (diamonds) T_{rad} at the cold resonance position from all edge ECE channels. (d) modeled T_{rad} for the ECE-I channels. The used T_{e} profile is plotted in all frames as a reference.

values differ from T_{e} not only in the optically thin region but also in the optically thick area. This is more obvious for the ECE-I system and indicates why the classical ECE approach [26] is also not applicable in the optically thick region. To avoid misinterpretation of the ECE-I measurements, it is therefore required to perform the forward modeling for all channels.

Especially, the implementation of the ray tracing is important to determine accurate (R, z) values for the 'warm' resonance position. This is illustrated in Fig. 9, which shows (R, z) of the 'warm' and the cold resonances. Remarkably, the majority of the ECE-I channels in this configuration probe the pedestal region. The channels in the optically thick region measure electrons located in this region due to the Doppler shift, whereas the SOL channels observe only the down-shifted radiation of the Maxwellian tail [26]. One should keep in mind that the Doppler shifted observation in the optically thick region is a feature due to the oblique LOS, whereas the feature of the SOL channels probing the pedestal region appear also for the case of perpendicular ECE views (see Ref. [49]). Since the SOL channels also contain valuable information, we also include them in our plasma response studies.

We use the 'warm' resonance positions as measurement positions and assume that they are constant during the rigid rotation. In principle, there are two possibilities which can modify the measurement position during the rigid rotation: (i) a change in the total magnetic field due the MP field could change the resonance position. The relative magnetic perturbation of the vacuum field in front of the MP-coils is $|\delta B|/|B| < 10^{-3}$ and around the midplane, it is even lower $|\delta B|/|B| < 10^{-4}$. The resulting difference

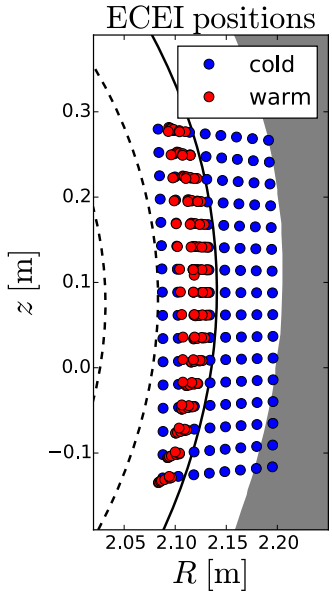

Figure 9. #30839 at 2.0 s. Cold and 'warm' resonance positions of all ECE-I channels. Differences in R and z between the cold and 'warm' resonance are apparent.

in the resonant position using the latter case is $\delta R < 0.2$ mm at $R \sim 2$ m. Thus, we assume that the resonance position is constant during the rigid rotations. (ii) Refraction due to a 3D geometry can additionally deflect the LOS ray and vary the measurement position. At the moment, the forward model of the ECE and the underlying ray tracing are not capable to deal with 3D flux surfaces. This additional toroidal angle is expected to be small, since $\delta\phi < arctan(|\delta B|/|B|) = 0.006°$. Even a relatively strong $n = 2$ flux surface displacement of 2 cm would result in an additional toroidal angle of only $\delta\phi \sim 1.1°$. Therefore, we neglect additional effects due to toroidal asymmetry on the ray tracing, which is justified by our estimation.

The combination of the forward modeling and ray tracing allows us to determine accurate (R, z) values of the 'warm' resonance position for the ECE and ECE-I diagnostics. These positions are used to calculate the straight field line angle and are essential for its interpretation. Of course, this approach is only valid if the D_ω is not bimodal and has only one dominant peak. This is the case for the ECE and in the majority of the ECE-I channels. Moreover, the forward modeling enables us to compare T_{rad} from the ECE measurements with calculated synthetic T_{rad} using the 3D equilibrium from VMEC. The generation of the synthetic data from VMEC will be elucidated in the following section.

4. Synthetic data from ideal MHD equilibrium (VMEC)

To compare measurements with an ideal MHD equilibrium, we use the free boundary version of VMEC [27]. VMEC uses a variational principle to determine the shape of a set of nested flux surfaces [50]. In the free boundary version, the external MP field enters the calculations by the boundary condition. The plasma energy (W_{MHD}) is then self-consistently minimized while the plasma boundary is varied to make the total pressure $\frac{1}{2\mu_0}B^2 + p = \frac{1}{2\mu_0}B_V^2$ continuous at the plasma boundary. The normal component of the vacuum field $\vec{B}_V$ vanishes such as $\vec{B}_V \cdot \vec{n}_p = 0$ ($\vec{n}_p$ = normal vector at the plasma boundary). The vacuum field $\vec{B}_V$ is produced by all external conductors (e.g. toroidal field coils, shaping and perturbations coils). The converged 3D equilibrium is a nonlinear solution of the ideal MHD model. This implies that (a) nonlinear coupling of toroidal modes is correctly represented and (b) the solution preserves inherently the original topology with nested flux surfaces, i.e. magnetic islands cannot be described. This latter property corresponds to perfect shielding of resonant field components. In contrast to other formulations, the variational method ensures this intrinsically, without the need to adjust surface currents at rational flux surfaces as done e.g. in perturbative codes.

4.1. Modelling inputs

The axisymmetric equilibrium reconstruction CLISTE from discharge #30839 at $t =$ 3.2 s serves as an input [51]. To reduce the influence of the MP-coils on the reconstruction, we choose a time point, when the MP-coils located closely to the B_Θ probes had almost zero current. This is demonstrated in Fig. 2, where the color scaling indicates the coil current at $t = 3.2$ s and the B_Θ probes are shown. The analyzed coil configuration is even parity with $n = 2$ and for the present plasma configuration with $q_{95} = -5.4$, the externally applied field is almost non-resonant. Fig. 10(a) illustrates the poloidal mode spectrum of $B_{\mathrm{r,res}}(\mathrm{n} = -2)$. Since ASDEX Upgrade has negative q in this case, only positive poloidal mode numbers are relevant for the negative toroidal mode components. To account for the components with the same helicity of the spectrum ($n = +2$), the illustrated $n = -2$ amplitudes are multiplied by a factor of 2. The external field is almost non-resonant, especially at the edge, which is emphasized by showing the poloidal mode spectrum of the $q \sim -5.0$ surface in Fig. 10(b). The resonant component of this surface is indicated by a red bar.

The pressure p, toroidal current and the safety factor q profile (Fig. 11) in the CLISTE equilibrium are restricted by kinetic profiles, a self-consistent bootstrap current in the edge gradient region and prescribed minimum q above 1 to avoid an unstable helical plasma core in VMEC, respectively. For the pressure constraints, the total pressure was determined at $t = 3.2$ s using various diagnostics like LIB, CXRS, Thomson scattering (TS), etc. The contribution from the fast particles is not taken into account, but this is usually negligible in the pedestal [52]. Because of the consideration of kinetic

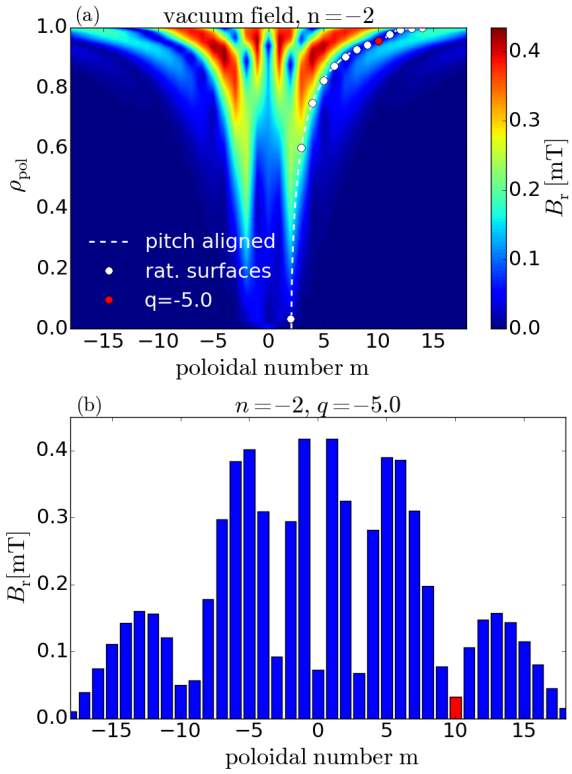

Figure 10. Mode spectra of the vacuum field using CLISTE equilibrium of #30839 at 3.2 s, (a) ρ_{pol} versus poloidal mode spectrum of the vacuum field perturbation. The pitch aligned components and the rational surfaces are shown as dashed line and white circles, respectively. (b) poloidal mode spectrum of $q \sim -5.0$ ($\rho_{pol} \sim 0.955$) surface in the pedestal region indicated as red circle in (a). The resonant component is illustrated as red bar. The applied field is almost non-resonant.

data, the bootstrap current causes a flattening in the q profile in the pedestal, Fig. 11. Since VMEC only deals with nested flux surfaces, the SOL is not considered and SOL currents were excluded in the reconstruction of the input equilibrium. Moreover, the flux surfaces were truncated at $\rho_{\rm pol} \sim 0.9999$ to avoid the singularity of the X-point.

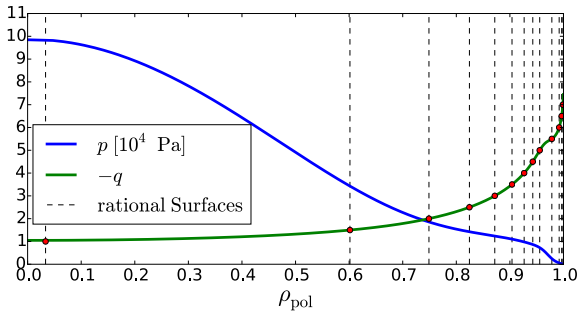

Figure 11. Total pressure p and the safety factor q are shown. Vertical lines indicate the rational surface positions for $n = 2$.

More details about the implementation of the VMEC code at ASDEX Upgrade is described in Ref. [14].

4.2. Justification of using ideal MHD

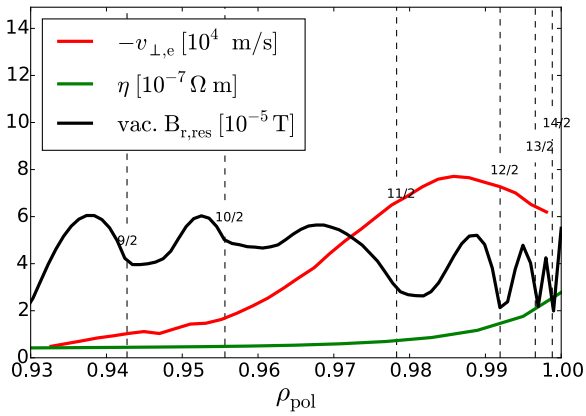

Figure 12. Perpendicular electron velocity $v_\perp$, Spitzer resistivity η and pitch aligned radial component of the vacuum field perturbation $B_{\mathrm{r,res}}$ are shown. Usually high $v_\perp$, low η and, for this case, low $B_{\mathrm{r,res}}$ are observed in the pedestal.

Since VMEC is an ideal MHD code with nested flux surfaces, no resistive MHD effects are included and no magnetic island can appear. The appearance of magnetic islands at the rational surfaces depends on the plasma resistivity η as well as on the velocity of the plasma frame expressed by the perpendicular electron velocity $v_{\perp,e}$ and the field strength of the resonant component of the external field $B_{\mathrm{r,res}}$ normal to the unperturbed flux surface. The velocity of the plasma frame in the pedestal is relatively high $v_{\perp,e}(q=-5.5) \sim -60$ km/s (Fig. 12) due to the dominant diamagnetic velocity [53]. Hence, it is expected that the, anyway small, pitch aligned components from the external field are screened. The resistivity in the pedestal region is low due to the high T_e. The calculated Spitzer resistivity is shown in Figure 12. Because of the low pitch aligned components, the high $v_{e,\perp}$ and low η, magnetic islands are unlikely in this case. In order to further justify our use of ideal MHD, we employed MARS-F calculations once with ideal MHD and twice with resistive MHD using Spitzer resistivity (η_{Spitzer}). The inputs for the MARS-F calculations are the same as for VMEC. The resulting magnetic perturbation of the total field between ideal and (Spitzer) resistive MHD differ only by maximal 0.01 mT in the poloidal mode spectra (not shown). In comparison to the values from the vacuum field calculations (see Fig. 10), this difference is very small. Moreover, the displacement of the resistive MHD calculations also exhibits no phase flip. This also underlines the use of ideal MHD

4.3. The VMEC calculation

To have sufficient accuracy of the resulting equilibrium, we used 1000 flux surfaces, 17 toroidal mode numbers ($n = -8, \ldots, 8$) and 25 poloidal mode numbers for one period. Because of $n = 2$, only one toroidal half was calculated. The toroidal ripple was not considered. One should also keep in mind that the $n = 0$ solution of the converged equilibrium can slightly vary from the CLISTE equilibrium. This difference can be balanced by shifting the plasma vertically and/or radially a few millimeters ($3 - 4$ mm). The properties of resulting 3D VMEC equilibrium are shown in Fig. 13. The displacement ξ_n is almost pitch aligned and strongest at the edge (Fig. 13(a)). The poloidal mode spectra can also be seen from a poloidal cut $\phi = 0°$ (Fig. 13(b)). The amplitude of the $n = -2$ displacement along the toroidal axis is shown in Fig. 13(c). The VMEC calculations show a pronounced $n = -2$ amplitude around the midplane at the LFS (Fig. 13(b)).

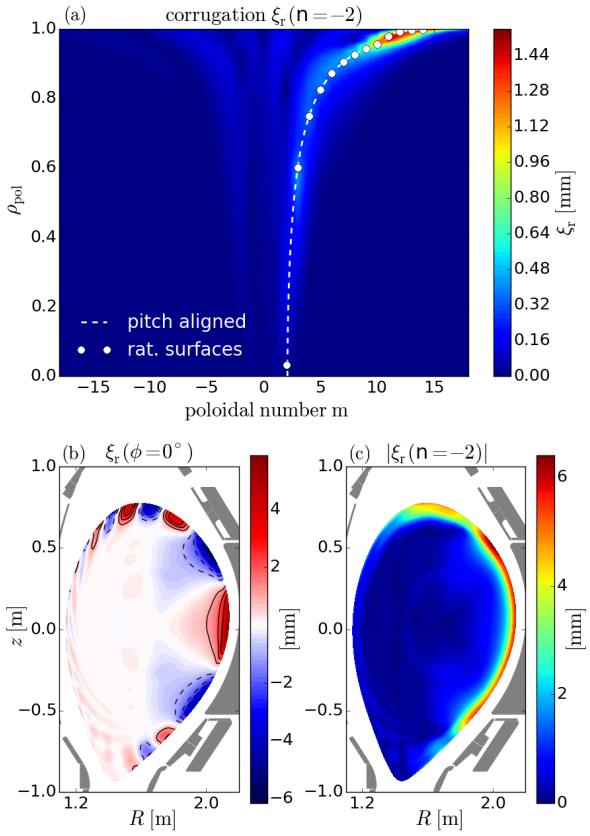

Figure 13. Corrugation from VMEC, (a) ρ_{pol} versus poloidal mode spectrum m of $n = -2$ component of the corrugation ξ_r, (b) poloidal cut of the corrugation at a toroidal angle of 0° and (c) amplitude of the $n = -2$ displacement along the toroidal axis. An edge kink response in the LFS midplane is apparent.

The VMEC calculations also exhibit a small $n = 4$ component, which can solely be attributed to the plasma response (not shown). The explanation is as follows: ASDEX Upgrade has 8 saddle coils in each row. Hence, the $n = 2$ perturbation can be described

as a rectangular function along the geometrical toroidal angle ϕ_{geo}. The Fourier series of a rectangular function solely consists of odd harmonics $(1, 3, 5, \dots)$. Consequently, the vacuum field solution of the $n = 2$ perturbation has exclusively toroidal mode numbers of $n = 2, 6, 10, \dots$. Additionally, the $n = 6$ component is increased due to the the aliasing effect from the $n = 2$ perturbation using 8 saddle coils ($n_{\text{aliasing}} = 8 - 2$). However, ASDEX Upgrade has no $n = 4$ component in the vacuum field spectra when applying an $n = 2$ perturbation. In DIII-D, for example, this is not the case. It has 6 saddle coils in each row, the aliasing effect causes an $n = 4$ component [54]. The combination of Ampere's law $\vec{j} = \vec{\nabla} \times \vec{B}$ and the plasma equilibrium $\nabla \vec{p} = \vec{j} \times \vec{B}$ introduces a non-linear ($\sim B^2$) behavior due to the plasma response. This non-linearity can lead to the appearance of additional toroidal mode numbers like $n = 4, 8, 12, \dots$. Therefore, a measured $n = 4$ component would prove a plasma response, but according to VMEC the maximum displacement of $n = 4$ amounts to $\xi_r(n = 4) \sim 0.2$ mm and is unlikely to be measured within the measurement accuracy.

4.4. Calculation of synthetic data

The output of VMEC is a 3D equilibrium calculated for one time point. To compare the toroidally localized measurements during a rigid rotation with this single 3D equilibrium, we developed synthetic diagnostics for the VMEC equilibrium. The most important steps to produce synthetic data are listed below:

(i) The currents of MP coils are used to map the timebase of the used diagnostic to the geometrical toroidal angle ϕ_{geo} in VMEC or vice versa. It is mapped in such way that the calculated ϕ_{geo} from the rotation corresponds to the toroidal position of the diagnostic at the time of the VMEC calculation ($t = 3.2$ s). Each slice in ϕ_{geo} can be correlated to a time point and vice-versa.

(ii) Because of small discrepancies between the input equilibrium and the axisymmetric component of the VMEC solution, the entire VMEC output is shifted by $R = 3$ mm, z = 4.5 mm to align the surfaces at the LFS. This allows us to compare vacuum field calculations using the input equilibrium with VMEC at the LFS.

(iii) The (R, z) positions of each channel are determined for each diagnostic and are assumed to be independent of time or rather ϕ_{geo}. In the case of ECE diagnostics, the 'warm' resonance positions are used.

(iv) T_e, T_i and n_e profiles before the MP phase are used to correlate the ρ_{pol} with T_e, T_i and n_e values assuming they are constant on the perturbed flux surface. Due to a slight increase in core n_e, the global T_e slightly decreases. To account for this, we add a time or rather ϕ_{geo} dependent scaling function. This function is a cubic spline and time traces from core channels were used to parametrize it.

(v) (R_i, z_i) of each channel i and ϕ_{geo} are used to deduce the corresponding $\rho^{\text{i}}_{\text{pol}}(\phi_{\text{geo}})$ values from the 3D VMEC equilibrium and therefore, also T_i and n_e values. To get synthetic T_{rad} values for ECE diagnostics, the electron cyclotron radiation transport

is solved using the slices of the poloidal flux surface at the corresponding ϕ_{geo} of the perturbed equilibrium. To solve radiation transport, T_e, n_e profiles as in step (iv) are used and each slice in ϕ_{geo} is assumed to be axisymmetric.

(vi) The VMEC output has no SOL flux surfaces. To complete the synthetic profiles in the SOL, the CLISTE equilibrium is used for flux surfaces for $\rho_{\text{pol}} > 1.04$. To allow a smooth transition between the perturbed VMEC and the axisymmetric CLISTE equilibrium, we simply use a 2D cubic spline to interpolate in-between.

All these steps allow us to compare quantitatively synthetic data from VMEC with measurements from ECE-I, ECE, CXRS and LIB. Moreover, we distinguish between the comparison of the amplitude and phase or rather poloidal mode structure of the flux surface displacement. We deduce both by fitting the measured and synthetic data to sine function with its harmonics.

5. Amplitude comparison

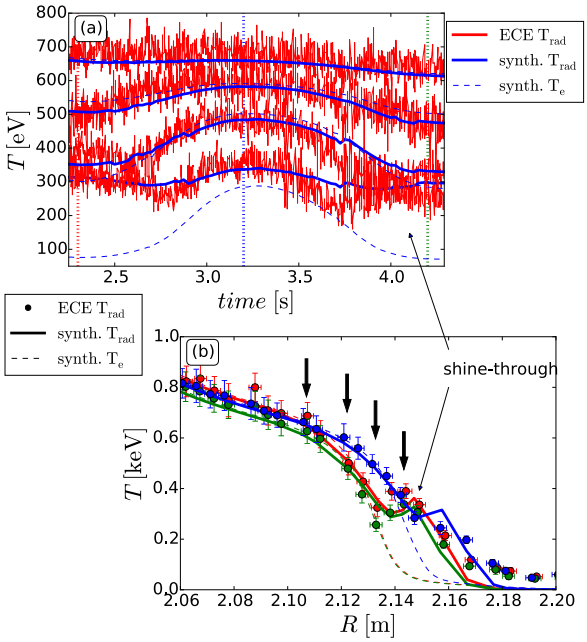

Figure 14. (a) Four time trace of the synthetic T_e (dashed), T_rad (solid blue), and the ECE diagnostic (solid red). Positions are indicated by arrows in (b). (b) Synthetic T_e (dashed), T_rad (solid) and measured T_rad profiles using the cold resonance position at three time points. Time windows are indicated by dotted vertical lines in (a). The shine through is marked. The synthetic and measured T_rad profiles are in reasonable good agreement.

In the following, we focus on the profile ECE system. Unlike the ECE-I, it has an absolute calibration and moreover, its spatial resolution is higher. Both are beneficial for the amplitude comparison, we will therefore concentrate on profile ECE system. But like every ECE system, its interpretation at the plasma edge can be challenging due to the transition from the optically thick to the optically thin plasmas (also discussed in Ref. [23]). This is demonstrated in Fig. 14 by comparing ECE measurements with synthetic T_rad and T_e profiles. Both, the time traces (Fig. 14(a)) and the corresponding profiles (Fig. 14(b)) from the ECE and the synthetic T_rad diagnostic match very well. The displacement is clearly visible in the profiles. Moreover, the synthetic T_rad profiles correctly describe some features of the shine-through. First, the peak slightly decreases due to the slight decrease in the global temperature. Second, the edge gradients are smaller at the maximum displacement and therefore, the shine-through peak is less pronounced. This is clearly seen in the measurements and also seen in the synthetic data, but less distinct. This indicates that VMEC slightly underestimates the change in the edge gradients. Moreover, the displacement seems also to be underestimated. As mentioned previously, channels in the far SOL measure a higher radiation than expected from the model. This is because the model does not take wall reflections into account,

which are particularly important at very low optical depth.

Because of the lack of density information in the 3D equilibrium at the ECE LOS, we are not able to determine T_e from ECE measurements in the presence of 3D perturbations. Therefore, we choose to compare ECE with synthetic T_rad profiles. Since we are dealing with multichannel profile diagnostics, it is possible to compare the displacement using either the entire profile information or it is also possible to use the amplitude information from the individual channels. Both possibilities will be discussed in the subsequent sections.

5.1. Using single channel information from ECE

This analysis is based on fitting each ECE channel using a sine function including its harmonics to extract the amplitude information. The shine-through limits the usage of T_rad to investigate edge perturbations. Moreover, it can lead to a misinterpretation of the amplitudes and phases from an $n = 2$ perturbation and can lead to a misapprehension of an '$n = 4$' component. This is illustrated in Fig. 15, where the amplitude and the phase of the synthetic T_rad, T_e and the ECE measurements are shown. Figure 15(a) shows the relative amplitudes ($\delta T_\mathrm{rad}/\mathrm{T_{rad}}$) of $n = 2$ and $n = 4$. The $n = 2$ amplitude of the synthetic T_e (blue dashed) peaks around the LCFS and is rapidly decaying towards the plasma core. The shine-through peak corrupts the simple analysis of phase and amplitude using T_rad from single channels. Especially the channels, which are located in the shine-through well, are affected. These channels view alternating the optically thin and thick region throughout the rotation. As a result, they show a reduced $n = 2$, an increased $n = 4$ amplitude and a distorted phase (channel around $R \sim 2.15$ m in Figure 15). This is clearly seen in the ECE measurements and well captured by the synthetic T_rad data. This measured '$n = 4$' component is most likely an artifact from the shine-through, because the $n = 4$ component, according to VMEC, amounts only to about 1/30 of the $n = 2$ component. On the positive side, this '$n = 4$' amplitude and the distorted phase can be used to exclude the corrupted channels without knowing its exact measurement position. We use this simple recipe to exclude ECE-I channels viewing the shine-through well. In the far SOL, discrepancies between measurements and synthetic T_rad are apparent. This is because these channels still observe some radiation due to wall reflections.

The amplitude and its decay of ECE and synthetic T_rad in the optically thick region are in good agreement. The amplitude is mainly measurable at the edge. This is because the perturbation is localized at the edge and the measurements of the displacement are larger in the large gradient region. Hence, the measured amplitude is a convolution between an edge perturbation and a localized T_e gradient. This makes a quantitative comparison using single channels difficult. The correct interpretation depends highly on the correct resonance positions of the ECE channels and on the correct local magnetic field strength.

In contrast to the amplitude comparison, the phase information is less dependent

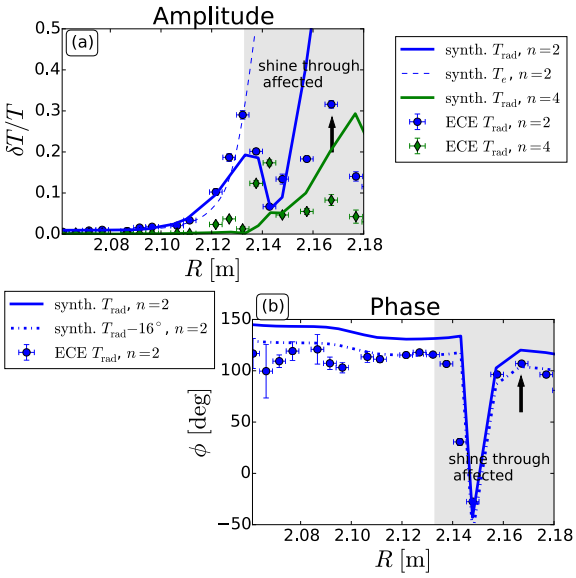

Figure 15. (a) relative amplitude of the $n = 2$ (blue) and $n = 4$ (green) component from the synthetic T_{rad} (solid) and the ECE measurements (circle) are shown. The $n = 2$ amplitude of synthetic T_{e} is also illustrated. (b) phase of $n = 2$ from synthetic T_{rad} and the ECE measurements. The phases systematically deviate by around 16° indicated by the dash-dotted line. The shine-through can distort significantly the amplitude and phase analysis.

on the radial position. The edge perturbation has large wavelengths at the LFS and the distortion penetrates straightly from the edge towards the core (see Fig. 13(b)). Thus, the phase is not changing much along the ECE LOS within the optically thick region. This is seen in the ECE measurements and the synthetic T_{rad} (Figure 15(b)). Moreover, the synthetic T_{rad} also successfully describes the phase flip at the edge, which is caused by the interplay between the displacement and the shine-through. Channels viewing only the optically thin plasma also contain the phase information from the pedestal. The ECE channels in the SOL showing a strong $n = 2$ component (arrow in Fig. 15) observes a similar phase as the pedestal channels, because they measure the down-shifted radiation of the electrons in the pedestal region. Slight differences between the channels can occur because they have different frequencies and therefore, slightly different rays.

The phase between the ECE T_{rad} and synthetic T_{rad} shows a systematic offset of $\Delta\phi \sim 16°$. This offset can be explained by the PSL response, which acts like an L/R low pass filter [32]. Although the MP field was rotated by only 0.5 Hz, the PSL causes a measurable phase delay. This is also inline with newly employed finite elements calculations of the MP coils and the PSL, which predict a phase delay in the midplane of $\Delta\phi_{\mathrm{upper}} \sim 14.3°$ regarding the upper coil set and $\Delta\phi_{\mathrm{lower}} \sim 11.2°$ for the lower one [30, 55]. The phase delay of the upper and lower coil set is different because of the different geometry with respect to the PSL.

5.2. Comparison using profile diagnostics

In the previous section, we used the amplitude information from single channels to compare it with synthetic data. But it is also possible to use the information from the entire edge profile. The displacement can be directly obtained from comparing two profiles at the phase with the maximum and the minimum displacement. Moreover, it also allows us to compare the displacement between the different profile diagnostics even if the measured plasma parameters are not the same. Figure 16 shows ECE, CXRS and LIB profiles at the time of maximum and minimum displacement. The corresponding synthetic data are also plotted. Due to the different toroidal and poloidal arrangement of the diagnostics, the times of the maximum and minimum vary for the different diagnostics. The agreement between the synthetic and the measured profiles are generally in good agreement. To get one quantity for the displacement, first, we fit the profiles at the maximum displacement using a spline. Then, this spline is only varied by a radial shift until the LSQ is minimized using the data at the minimum displacement. This is more robust and also allows us to account for the shape of the shine-through in the T_{rad} profile. Because of the shine-through and dominating passive lines, the ECE and the CXRS data from the SOL are not used for this procedure. The uncertainties due to the change in the gradients are also reflected in the uncertainties of the determined distortion. The same procedure was also applied to the synthetic data. The displacements derived from this procedure are also given in Fig. 16. ECE and CXRS deliver very similar displacements, but both exhibit slightly larger distortions than expected from VMEC. In the case of LIB, this difference between the measurements and VMEC is more pronounced.

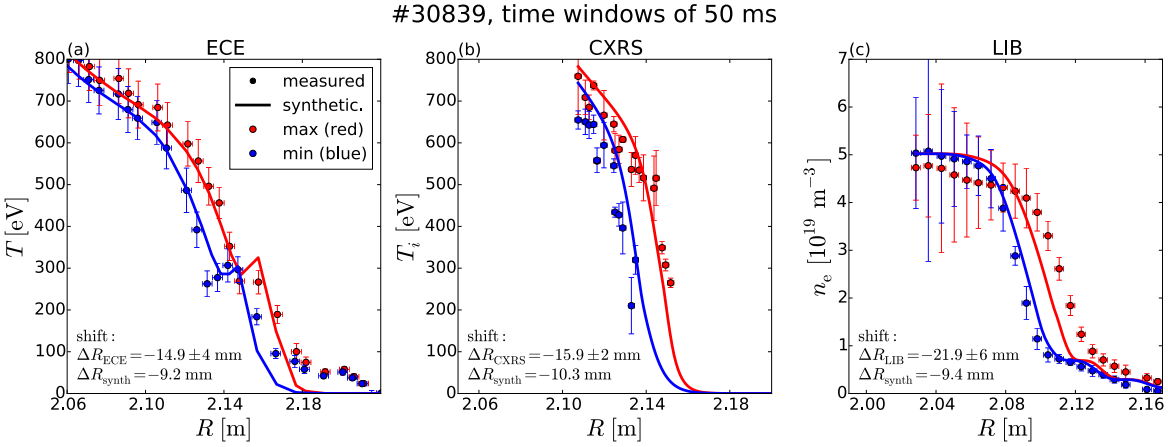

Figure 16. Profiles from (a) ECE (b) CXRS and (c) LIB. Measured (circles) and synthetic (solid) profiles at the maximum (red) and minimum displacement (blue) of each diagnostic. The analyzed time windows are 50 ms. The derived displacements are given in the left bottom corner. ECE and CXRS observe the same displacement, whereas the one measure by LIB is slightly larger.

Unlike ECE and CXRS, the LIB diagnostic has a decreasing sensitivity towards

the plasma core. But it is an excellent diagnostic to determine changes of the separatrix position. Assuming a constant separatrix density determined from Fig. 5) during the rigid rotation, the separatrix position can be easily tracked along the LIB. Figure 17 illustrates (i) the separatrix position determined from the LIB diagnostic ($n_{e,sep} \sim 1.3 \cdot 10^{19}$ m^{-3}), (ii) the outermost boundary of the VMEC equilibrium and (iii) the boundary from vacuum field solution is indicated by the color scaling using the connection length L_c of the stable manifold (see Ref. [18]). Both, (ii) and (iii) are calculated along the LIB LOS. The distortion of the VMEC solution exceeds the vacuum calculations by a few millimeters due to the plasma amplification. The sinusoidal is well seen in the measurements und agrees qualitatively. This comparison indicates a larger displacement than predicted by VMEC and is also consistent with the measurements shown in Fig. 17(c).

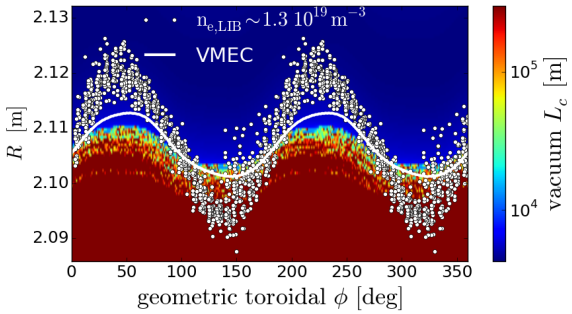

Figure 17. Circles are the estimated separatrix from LIB using a density of $1.3 \cdot 10^{19}$ m^{-3}. Solid line is the outermost flux surface from VMEC along the LIB LOS and the color scaling indicates the connection length L_C from the vacuum field calculations. LIB data exceeds the VMEC and the vacuum field calculations. LIB data is shifted radially inwards by 2 mm.

5.3. Discussion of amplitude comparison

A quantitative amplitude comparison using single ECE channels is challenging due to the dependencies on the measurement positions and the shine-through. Small variations in the position can have large influence on its interpretation. Despite these difficulties, the decay of the distortion towards the plasma core agrees very well between the ECE T_{rad} and the synthetic T_{rad}. Using the relative amplitude from single channels makes it difficult to compare different diagnostics measuring different plasma parameters. For this purpose, it is more useful to determine the displacement by aligning the entire edge profiles. This method is more stable and allows us to compare directly the displacement. Therefore, we conclude that the amplitude information from single ECE channels should be considered with caution, especially in the case of ECE-I due to the additional oblique angles and the lower spatial resolution.

All edge profile diagnostics around the LFS midplane exhibit a modulation, which exceeds slightly the calculations from VMEC and therefore the one from the vacuum field

as well. In principle, the plasma position control could artificially amplify or mitigate the distortion, which depends on the relative phase between the position of the B_Θ arrays and the used profile diagnostics (discussed in Ref. [22]). We can exclude this in the midplane for two reasons. First, CXRS and 1D-ECE measure the same amplitude at different toroidal phases (see time traces Fig. 4). Second, the CXRS system is in the midplane on the opposite side of the B_Θ array (see Fig. 2). A feedback controlled system solely based on measurements of one toroidal position would counteract the 3D distortion [22] and, therefore, the modulation at the position of the CXRS system would be compensated. Because of the fact that the displacement from edge CXRS exceeds the one expected from VMEC as well, we assume that the plasma position control system does not artificially amplify the measured modulation in the midplane. The position control system of ASDEX Upgrade also uses toroidal flux loops for the feedback control system, which seem to mitigate the effect of the MP-field on the control system in comparison to other devices like MAST [22]. However, small changes in the shape due to the control system can certainly not be excluded, which could explain that LIB measures a larger displacement than CXRS and ECE.

VMEC seems to slightly underestimate the displacement in the midplane. A quantitive comparison of MARS-F employing the resistive as well as the ideal MHD model with VMEC using the identical inputs show very similar displacement values. This points towards the assumption that the used input parameters rather than the underlying MHD model are the cause for this underestimation. As already mentioned in section 4.3, the used pressure profile was determined by aligning various diagnostics at one time point during the MP-phase. The resulting total pressure has experimental uncertainties because the various used diagnostics are toroidally separated. As shown in Fig. 5, the gradients can vary depending on the toroidal phase. Since the amplitude of the displacement is very sensitive to the pressure gradient, a lower pressure gradient can lead to a smaller displacement. For further details on the sensitivity of the displacement on the pressure profile and hence, the plasma beta, we refer to the sensitivity study in Ref. [14].

Unlike the amplitude comparison, the profile ECE indicates that the phase measurements are more robust. This is because of its small dependence on its radial position in the midplane.

6. Poloidal mode structure comparison

The amplitude comparison indicates a beta amplified kink response since the VMEC and measured modulation amplitude exceeds the one from the vacuum field calculations. According to plasma response calculations, the amplified magnetic perturbation shows a dominant non-resonant component ($|m| > |nq|$) in the magnetic structure. To investigate if this non-resonant behavior is also seen in the ECE-I system, we make use of its poloidal resolution and compare measured data to VMEC calculations.

6.1. ECE-I vis-a-vis VMEC

Figure 18 shows the comparison between the measured (diamonds) and the synthetic ECE-I (circles) data. To avoid corruption from the shine-through well, channels are discarded which measure a significant '$n = 4$' ($\delta T_{\mathrm{rad}}/T_{\mathrm{rad}}(n = 4) > 0.05$) component. We only use channels with a significant $n = 2$ component ($\delta T_{\mathrm{rad}}/T_{\mathrm{rad}}(n = 2) > 0.085$). The few channels, which have their cold resonance position in the optically thin region and fulfill the conditions, are also considered (green diamonds). Because of these conditions we only consider channels, which view either the optically thick or thin region throughout the entire rigid rotation.

All selected channels from ECE-I and their corresponding synthetic channels are fitted using the LSQ fit of a sine function considering higher harmonics. The ρ_{pol} values of the used channels ranges from 0.95 to 0.981 and their mean value is 0.968, which is the $q \sim 5.35$ surface. To illustrate the comparison of the poloidal mode structure between the measurements and the synthetic data, we plot the straight field line angles of the channels using the $q \sim 5.35$ surface versus the phase determined from the sine fits in Figure 18. We use the 'warm' resonance position to calculate the straight field line angles for channels with the cold resonance position in the optically thick (blue diamonds) and thin (green diamonds) regions. The measured and the synthetic data agree very well. Using only the $q \sim 5.35$ surface to determine the poloidal mode number, one gets $m_{ECE-I} \sim 9.83 \pm 0.98$ for ECE-I and $m_{synth} \sim 10.72 \pm 0.63$ for the synthetic data. Furthermore, using only the ECE-I channels in the optically thick does not change strongly the result. One should also keep in mind that the q-profile contains also uncertainties, since the initial equilibrium calculation is constrained by measured kinetic profiles.

Nevertheless, the synthetic and the measured data point towards an almost resonant response $m_{pitch} \sim 10.7$. In fact, the m_{ECEI} tends to be even lower than the pitch aligned mode number. This is in contradiction to the non-resonant response with $|m| > |nq|$ expected from the magnetic structure. This discrepancy originates from a difference in the poloidal mode number between the magnetic perturbation and the flux surface displacement, which will be discussed in the following section.

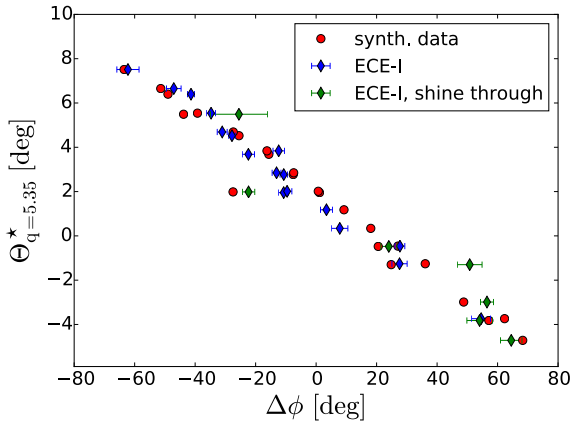

Figure 18. Straight field line angle of the $q = 5.35$ flux surface versus the derived phase difference using $\Delta\phi = \phi - < \phi >$. ECEI data from optically thick (blue diamonds) and thin (green diamonds) plasma regions are in good agreement with synthetic data from VMEC (red circles).

6.2. Corrugation versus magnetic perturbation

To compare the flux surface displacement with the magnetic perturbation, we used a modified version of the MFBE code [56] (described in [57]) to calculate the magnetic perturbation. In the following, we compare the mode spectra of the magnetic perturbation and the corrugation from VMEC and from MARS-F using ideal MHD. The poloidal mode structure is determined by calculating an axisymmetric straight field line coordinate system using the equilibria from MARS-F and VMEC. Since these straight field line coordinate systems can deviate, we compare the poloidal mode spectra of the vacuum field perturbation using them. Figures 19(a) and 19(d) show the vacuum field perturbation using the coordinate system from VMEC and MARS-F, respectively. The spectra from the vacuum field calculations agree very well and are also consistent to the calculations shown in Fig. 10, where the CLISTE equilibrium was used. Note, only the $n = -2$, $m > 0$ components are displayed. As previously, to account for the identical $n = 2$ and $m < 0$ components, the mode spectra are simply multiplied by a factor of 2.

The total field from VMEC as well as from MARS-F show a beta amplified kink response, which is situated at $|m| > |nq|$. This has been reported previously [15, 17, 58, 54] and has also been experimentally verified using probe measurements [17, 59]. The lowest values of the total field are around the resonant surfaces, which is expected from ideal MHD. On the contrary, the mode spectra of the flux surface displacement does not indicate such pronounced non-resonant components. The structures are almost pitch aligned and exactly resonant around the pedestal top [60]. The poloidal mode structure of the corrugation from MARS-F and VMEC are also in good agreement with the ECEI measurements (diamond) within their uncertainties. The amplitudes of the corrugation from both codes agree quantitatively, whereas the

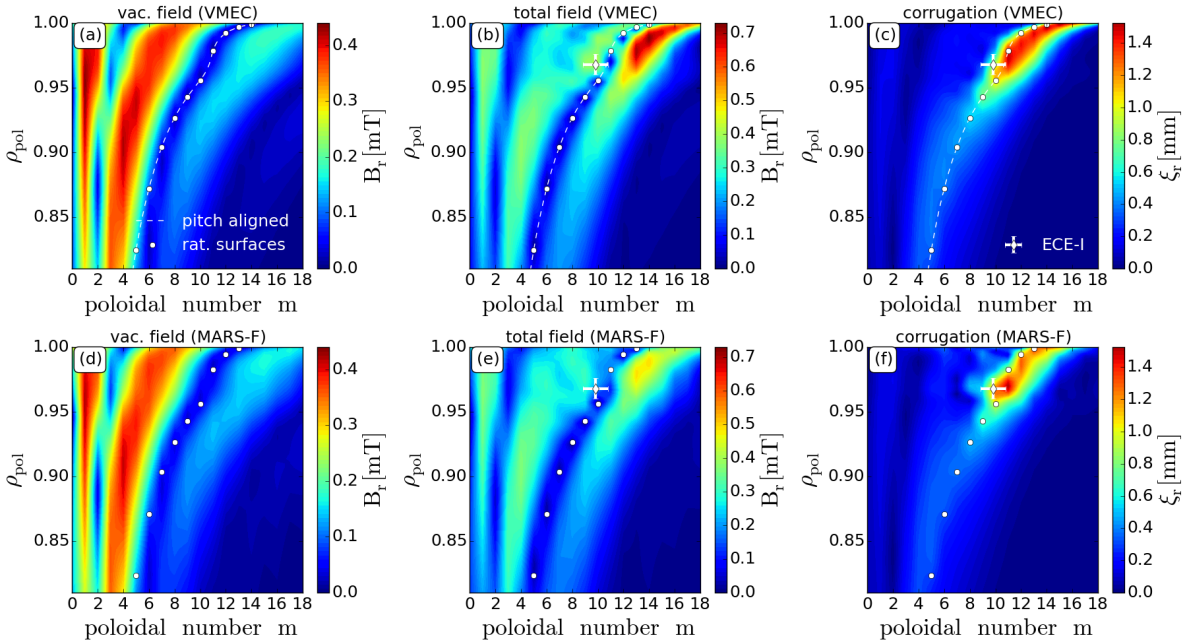

Figure 19. The $n = -2$ poloidal mode spectrum of (a) vacuum field, (b) total field, (c) the corrugation from VMEC and (d) vacuum field, (e) total field, (f) the corrugation from MARS-F. Note, there is no difference in the color scaling between VMEC and MARS-F, but it differs for the two parameters. The difference in the poloidal mode spectrum between total field and corrugation is apparent in both codes.

magnetic perturbations agree qualitatively and some differences in absolute values are apparent. Deviations from exactly zero resonant components at rational surfaces due to ideal MHD can arise from numerical limitations and/or from the treatment of sheet currents on rational surfaces [61]. Detailed quantitative comparisons between MARS-F and VMEC are beyond the scope of this paper.

6.3. Discussion of poloidal mode structure

While the calculated magnetic structure is non-resonant, the measured corrugation using ECE-I shows an almost resonant response. These observations are confirmed by VMEC and MARS-F calculations. This is a seeming contradiction, since the total field is the important parameter, which determines the displacement. Hence, one would expect that they have the same mode structure. In the following, we will briefly show that this difference can already be explained by simple ideal MHD calculations.

In linear MHD, the linearized magnetic perturbation $\vec{B} = \vec{B_0} + \vec{B_1}$ is related with the surface displacement $\vec{\xi}$ via [62]:

$$\vec{B_1} = \vec{\nabla} \times (\vec{\xi} \times \vec{B_0}). \tag{2}$$

Assuming a cylindrical plasma (r, Θ, z), the displacement ξ_r and magnetic field

perturbation B_r normal to the axisymmetric flux surface relate:

$$B_r = \frac{B_\Theta}{r}\frac{\partial \xi_r}{\partial \Theta} + B_\phi \frac{\partial \xi_r}{\partial z}, \tag{3}$$

where B_Θ and B_ϕ are the poloidal and toroidal magnetic component, respectively. Using a periodic distortion $\xi_\mathrm{r} = \xi_\mathrm{a}\ \mathrm{e}^{\mathrm{i}(\mathrm{m}\Theta - \frac{\mathrm{n}}{\mathrm{R}}\mathrm{z})}$ and the resonant condition $q = \frac{m}{n} = \frac{r}{R}\frac{B_\phi}{B_\Theta}$, one gets the following relation at rational surfaces:

$$B_r = i\frac{B_\Theta}{r}\,(m - nq)\,\xi_r \rightarrow \xi_r \propto \frac{B_r}{m - nq} \tag{4}$$

Consequently, ξ_r maximizes at rational surfaces in cylindrical plasmas [63]. In the case of an elongated toroidal plasma, the Jacobian J of the transformation from the torus coordinate system to the cylindrical system adds to the relation in Equ. 4 and hence, the left hand side is replaced by JB_r. Since J also causes additional coupling between the different harmonics $\Delta m = 0, 1, 2$, the product JB_r is a convolution of J and B_r over all poloidal harmonics. Thus, the relation between B_r and ξ_r is not a relation between individual harmonics anymore. Nevertheless, the $\frac{1}{m-nq}$ dependence in Equ. 4 is the underlying reason for ξ_r to be primarily resonant (Fig. 19(c,f)).

In summary, linear perturbative ideal MHD gives a reasonable explanation for the differences in the mode structure between the surface displacement and magnetic perturbation. Initially, one idea of measuring the poloidal mode number was to distinguish resonant resistive MHD response from non-resonant ideal MHD response. Since this non-resonant ideal MHD response is practically resonant in the displacement, this method is not suitable to disentangle resistive from ideal MHD response.

7. Conclusions

The combination of a rigid rotating MP-field and toroidally localized diagnostics provide a useful tool to measure the plasma surface distortion. This analysis relies on stable plasma conditions during the rigid rotation and on a high resolution of the used diagnostics. Especially, ECE diagnostics deliver informations about the plasma response within the confined region, whereas measurements around the separatrix are difficult to interpret. Additional oblique angles of the LOS complicate the interpretation of the ECE measurements. It was therefore necessary to combine ray tracing with forward modeling of the radiation transport. The calculation of 'warm' resonance positions (calculated maximum of the observed intensity distribution) is useful to estimate the real measurement position. The ideal MHD equilibrium code VMEC was used to model the 3D plasma surface displacement and synthetic diagnostics were developed to compare the measurements with VMEC.

A quantitative comparison of the displacement amplitude appears to be challenging. One can either use the single channel information and/or the entire profile information for the comparison. The first one is easier to realize, but implies the difficulty of the large sensitivity on the measurement position and of the incomparability between the

different diagnostics. Hence, we conclude that the use of the entire profile appears to be more robust.

The comparisons of the displacement between synthetic and measured data are in reasonable agreement. The modeling underestimates only slightly the amplitude of the distortion. Since MARS-F and VMEC exhibit very similar displacements, one plausible explanations for this minor underestimation could also be the uncertainties in the input parameters, like the pressure profile or the shape of the input equilibrium [64]. One should also keep in mind the role of the plasma position control during the rigid rotation. In the case of ASDEX Upgrade, the effect of the control system seems to be relatively small in the midplane due to the implementation of toroidal flux loops in the used reconstruction. In conclusion, not only the measurements of the amplitude require a careful treatment, but also input parameters for the modeling in the presence of non-axisymmetric MPs.

The usage of ECE-I shed some light onto the poloidal mode structure of the plasma response within the pedestal. Differences in the mode structure between the magnetic and the flux surface perturbation are apparent in plasma response calculations using MARS-F and VMEC. Whereas the poloidal mode structure of the magnetic perturbation is non-resonant, the corrugation expected from ideal MHD is almost resonant [63]. Hence, it is not possible to use the poloidal mode number from the displacement to disentangle ideal from resistive MHD response (resistive is always resonant).

MARS-F calculations of a differential phase scan [20] indicate that a variation in differential phase angle $\Delta\phi_{\mathrm{ul}}$ excites the modes with the same poloidal mode numbers. Either the low-n peeling at the X-point or/and the core kink mode LFS midplane are excited. Hence, the poloidal mode structure of the magnetic structure ($|m| > |nq|$) and the flux surface displacement remains and only the amplitude of the exited modes varies with $\Delta\phi_{\mathrm{ul}}$. This should result in a different behavior of the displacement around X-point and midplane. Furthermore, the pressure profile and its gradients are crucial inputs for the resulting amplitude of the displacement. Therefore, the impact of the pressure profile and the differential phase angle $\Delta\phi_{\mathrm{ul}}$ on the displacement amplitude, although experimentally challenging, will be subject of future investigations.

8. Acknowledgement

The authors would like to thank V. Igochine and E. Wolfrum for fruitful discussions. F. M. Laggner is a fellow of the Friedrich Schiedel Foundation for Energy Technology. This work has been carried out within the framework of the EUROfusion Consortium and has received funding from the Euratom research and training programme 2014-2018 under grant agreement No 633053. The views and opinions expressed herein do not necessarily reflect those of the European Commission.

[1] T. E. Evans et al. Suppression of Large Edge-Localized Modes in High-Confinement DIII-D Plasmas with a Stochastic Magnetic Boundary. *Physical Review Letters*, 92:235003, June 2004.

[2] Y. Liang et al. Active Control of Type-I Edge-Localized Modes with $n = 1$ Perturbation Fields in the JET Tokamak. *Physical Review Letters*, 98:265004, June 2007.

[3] W. Suttrop et al. First Observation of Edge Localized Modes Mitigation with Resonant and Nonresonant Magnetic Perturbations in ASDEX Upgrade. *Physical Review Letters*, 106(22):225004, 2011.

[4] T. E. Evans et al. RMP ELM suppression in DIII-D plasmas with ITER similar shapes and collisionalities. *Nuclear Fusion*, 48(2):024002, 2008.

[5] Y. Sun et al. Modeling of non-axisymmetric magnetic perturbations in tokamaks. *Plasma Physics and Controlled Fusion*, 57(4):045003, 2015.

[6] Y. M. Jeon et al. Suppression of Edge Localized Modes in High-Confinement KSTAR Plasmas by Nonaxisymmetric Magnetic Perturbations. *Physical Review Letters*, 109:035004, 2012.

[7] A. Kirk et al. Understanding edge-localized mode mitigation by resonant magnetic perturbations on MAST. *Nuclear Fusion*, 53(4):043007, 2013.

[8] W. Suttrop et al. Studies of magnetic perturbations in high confinement mode plasmas in asdex upgrade. *AEA Int. Conf. on Fusion Energy (St Petersburg, Russia, 2014) EX/P1-23*, 2014.

[9] A. Kirk et al. Effect of resonant magnetic perturbations on low collisionality discharges in MAST and a comparison with ASDEX Upgrade. *Nuclear Fusion*, 55(4):043011, 2015.

[10] M. Garcia-Munoz et al. Fast-ion losses induced by ELMs and externally applied magnetic perturbations in the ASDEX Upgrade tokamak. *Plasma Physics and Controlled Fusion*, 55(12):124014, 2013.

[11] C. Paz-Soldan et al. Observation of a Multimode Plasma Response and its Relationship to Density Pumpout and Edge-Localized Mode Suppression. *Physical Review Letters*, 114:105001, 2015.

[12] Y. Q. Liu et al. Feedback stabilization of nonaxisymmetric resistive wall modes in tokamaks. I. Electromagnetic model. *Physics of Plasma*, 7(9):3681, 2000.

[13] F. Orain et al. Non-linear MHD modeling of edge localized mode cycles and mitigation by resonant magnetic perturbations. *Plasma Physics and Controlled Fusion*, 57(1):014020, 2015.

[14] E. Strumberger et al. MHD instabilities in 3D tokamaks. *Nuclear Fusion*, 54(6):064019, 2014.

[15] D. A. Ryan et al. Toroidal modelling of resonant magnetic perturbations response in ASDEX-Upgrade: coupling between field pitch aligned response and kink amplification. *Plasma Physics and Controlled Fusion*, 57(9):095008, 2015.

[16] F. Orain, M. Hoelzl, E. Viezzer, M. Dunne, M. Becoulet, P. Cahyna, G. T. A. Huijsmans, J. Morales, M. Willensdorfer, W. Suttrop, A. Kirk, S. Pamela, E. Strumberger, S. Guenter, A. Lessig, the ASDEX Upgrade Team, and the EUROfusion MST1 Team. Non-linear modeling of the plasma response to RMPs in ASDEX Upgrade. *submitted to Nuclear Fusion*, February 2016.

[17] M J Lanctot et al. Measurement and modeling of three-dimensional equilibria in DIII-D. *Physics of Plasma*, 18(5):056121, 2011.

[18] R. A. Moyer et al. Measurement of plasma boundary displacement by n= 2 magnetic perturbations using imaging beam emission spectroscopy. *Nuclear Fusion*, 52(12):123019, 2012.

[19] M. W. Shafer et al. Plasma response measurements of non-axisymmetric magnetic perturbations on DIII-D via soft x-ray imaginga). *Physics of Plasmas (1994-present)*, 21(12):–, 2014.

[20] Y. Q. Liu et al. Toroidal modelling of RMP response in ASDEX Upgrade: coil phase scan, q95 dependence, and toroidal torques. *accepted in NF*, 2016.

[21] I. T. Chapman et al. Three-dimensional corrugation of the plasma edge when magnetic perturbations are applied for edge-localized mode control in MAST. *Plasma Physics and Controlled Fusion*, 54(10):105013, 2012.

[22] I. T. Chapman et al. The effect of the plasma position control system on the three-dimensional distortion of the plasma boundary when magnetic perturbations are applied in MAST. *Plasma Physics and Controlled Fusion*, 56(7):075004, 2014.

[23] B. J. Tobias et al. Boundary perturbations coupled to core 3/2 tearing modes on the DIII-D tokamak. *Plasma Physics and Controlled Fusion*, 55(9):095006, 2013.

[24] B. J. Tobias et al. Non-axisymmetric magneto- hydrodynamic equilibrium in the presence of internal magnetic islands and external magnetic perturbation coils. *Plasma Physics and*

Controlled Fusion, 55(12):125009, 2013.

[25] J. K. Park et al. Computation of three-dimensional tokamak and spherical torus equilibria. *Physics of Plasma*, 14(5), 2007.

[26] S. K. Rathgeber et al. Estimation of edge electron temperature profiles via forward modelling of the electron cyclotron radiation transport at ASDEX Upgrade. *Plasma Physics and Controlled Fusion*, 55(2):025004, 2013.

[27] S. P. Hirshman et al. Three-dimensional free boundary calculations using a spectral Green's function method. *Computer Physics Communications*, 43(1):143–155, 1986.

[28] R. Fischer et al. Spatiotemporal response of plasma edge density and temperature to non-axisymmetric magnetic perturbations at ASDEX Upgrade. *Plasma Physics and Controlled Fusion*, 54(11):115008, 2012.

[29] J. C. Fuchs et al. Investigation of the boundary distortions in the presence of rotating external magnetic perturbations on ASDEX Upgrade. *41th EPS Conference on Plasma Phys.*, 2014.

[30] W. Suttrop et al. In-vessel saddle coils for MHD control in ASDEX Upgrade. *Fusion Engineering and Design*, 84(2–6):290–294, 2009.

[31] M. Teschke et al. Electrical Design Of The Inverter System BUSSARD For ASDEX Upgrade Saddle Coils. *Fusion Engineering and Design / 28th Symposium on Fusion Technology (SOFT 2014) (SOFT 2014) Fusion Engineering and Design / 28th Symposium on Fusion Technology (SOFT 2014) (SOFT 2014)*, 2014.

[32] W. Suttrop et al. Physical description of external circuitry for Resistive Wall Mode controlin ASDEX Upgrade. *36th EPS Conference on Plasma Phys. Sofia*, 33E:1–4, 2009.

[33] W. Suttrop et al. Studies of edge localized mode mitigation with new active in-vessel saddle coils in ASDEX Upgrade. *Plasma Physics and Controlled Fusion*, 53(12):124014, 2011.

[34] M. Maraschek et al. Measurement and impact of the n=1 intrinsic error field at ASDEX Upgrade. *40th Conf.EPS Plasma Phys. (Espoo, 1–5 July 2013)*, 2014.

[35] E. Viezzer et al. High-resolution charge exchange measurements at ASDEX Upgrade. *Review of Scientific Instruments*, 83(10):103501, 2012.

[36] M. Willensdorfer et al. submitted. *Review of Scientific Instruments*, 2011.

[37] M. Willensdorfer et al. Characterization of the Li-BES at ASDEX Upgrade. *Plasma Physics and Controlled Fusion*, 56(2):025008–10, January 2014.

[38] B. Carli. Design of a Blackbody Reference Standard for the Submillimeter Region. *Microwave Theory and Techniques, IEEE Transactions on*, 22(12):1094–1099, 1974.

[39] H. J. Hartfuss et al. Heterodyne methods in millimetre wave plasma diagnostics with applications to ece, interferometry and reflectometry. *Plasma Physics and Controlled Fusion*, 39(11):1693, 1997.

[40] I. Classen et al. 2D electron cyclotron emission imaging at ASDEX Upgrade (invited). *Review of Scientific Instruments*, 81(10):10D929–6, 2010.

[41] I. Classen et al. Dual array 3D electron cyclotron emission imaging at ASDEX Upgradea). *Review of Scientific Instruments*, 85(11), 2014.

[42] Y. Gao et al. Effects of 3D magnetic perturbation on divertor heat load redistribution on ASDEX Upgrade . *42nd EPS Conference on Plasma Phys. Lissabon*, 39E:1–4, 2015.

[43] A. D. Turnbull et al. Plasma response models for non-axisymmetric perturbations. *Nuclear Fusion*, 52(5):054016, 2012.

[44] R. Fischer et al. Integrated data analysis of profile diagnostics at asdex upgrade. *Fusion science and technology*, 58(675–682), 2010.

[45] S. S. Denk et al. Interpretation of electron cyclotron emission in the presence of kinetic effects and wave-plasma interaction at ASDEX Upgrade. *submitted to Plasma Physics and Controlled Fusion*, 2016.

[46] S. S. Denk et al. Modelling of oblique electron cyclotron emission diagnostics. *in preparation for review of scientific instruments*, 2016.

[47] E. Poli et al. TORBEAM, a beam tracing code for electron-cyclotron waves in tokamak plasmas.

Computer Physics Communications, 136(1–2):90–104, 2001.

[48] M. Sato et al. Relativistic Down-Shift Frequency Effect on the Application of Electron Cyclotron Emission Measurements to Medium Temperature Tokamak Plasmas *. *Japanese Journal of Applied Physics*, 34(6A):L708, 1995.

[49] B. J. Tobias et al. ECE-imaging of the H-mode pedestal (invited). *Review of Scientific Instruments*, 83(10), 2012.

[50] S. P. Hirshman et al. Steepest-descent moment method for three-dimensional magnetohydrodynamic equilibria. *Physics of Fluids*, 26(12):3553, 1983.

[51] P. J. McCarthy et al. Identification of edge-localized moments of the current density profile in a tokamak equilibrium from external magnetic measurements. *Plasma Physics and Controlled Fusion*, 54(1):015010, 2012.

[52] M. G. Dunne et al. Measurement of neoclassically predicted edge current density at ASDEX Upgrade. *Nuclear Fusion*, 52(12):123014, 2012.

[53] E. Viezzer et al. Evidence for the neoclassical nature of the radial electric field in the edge transport barrier of asdex upgrade. *Nuclear Fusion*, 54(1):012003, 2014.

[54] S. R. Haskey et al. Linear ideal MHD predictions for n = 2 non-axisymmetric magnetic perturbations on DIII-D. *Plasma Physics and Controlled Fusion*, 56(3):035005, 2014.

[55] W. Suttrop. Finite elements calculations from the saddle coils and the PSL. *private communication*, 2016.

[56] E. Strumberger et al. Finite- magnetic field line tracing for helias configurations finite- magnetic field line tracing for helias configurations. *Nuclear Fusion*, 37(19), 1997.

[57] E. Strumberger et al. Numerical computation of magnetic fields of two- and three-dimensional equilibria with net toroidal current. *Nuclear Fusion*, 42(7):827, 2002.

[58] M J Lanctot et al. Sustained suppression of type-I edge-localized modes with dominantly n = 2 magnetic fields in DIII-D. *Nuclear Fusion*, 53(8):083019, 2013.

[59] J. D. King et al. Three-dimensional equilibria and island energy transport due to resonant magnetic perturbation edge localized mode suppression on DIII-D. *Physics of Plasma*, 22(11), 2015.

[60] Samuel A Lazerson, Joaquim Loizu, Steven Hirshman, and Stuart R Hudson. Verification of the ideal magnetohydrodynamic response at rational surfaces in the VMEC code. *Physics of Plasma*, 23(1):012507, 2016.

[61] A. Reiman et al. Tokamak plasma high field side response to an n = 3 magnetic perturbation: a comparison of 3D equilibrium solutions from seven different codes. *Nuclear Fusion*, 55(6):063026, 2015.

[62] J. Freidberg. *Ideal MHD, page 337*. Cambridge University Press, 2014.

[63] J. Loizu. et al. Pressure-driven amplification and penetration of resonant magnetic perturbations. *submitted to physics of plasmas*, 2016.

[64] L. Li et al. Modelling plasma response to RMP fields in ASDEX-Upgrade with varying edge safety factor and triangularity. *submitted to Nuclear Fusion*, 2016.